Princeton Plasma Physics Laboratory

PPPL-5355

Feasibility study of 01-mode ECRH in NSTX-U startup plasma

F.M. Poli

February 2017

Prepared for the U.S.Department of Energy under Contract DE-AC02-09CH11466.

Princeton Plasma Physics Laboratory
Report Disclaimers

Full Legal Disclaimer

Trademark Disclaimer

PPPL Report Availability

Princeton Plasma Physics Laboratory:

http://www.pppl.gov/techreports.cfm

Office of Scientific and Technical Information (OSTI):

http://www.osti.gov/scitech/

Related Links:

U.S. Department of Energy

U.S. Department of Energy Office of Science

U.S. Department of Energy Office of Fusion Energy Sciences

Feasibility study of O1-mode ECRH in NSTX-U startup plasma

N A Lopez[1] and F M Poli[2]

[1] Department of Astrophysical Sciences, Princeton University, Princeton, New Jersey 08544, USA

[2] Princeton Plasma Physics Laboratory, Princeton, NJ 08543, USA

E-mail: nlopez@pppl.gov

Abstract. Recently published scenarios for fully non-inductive startup and operation on the National Spherical Torus eXperiment Upgrade (NSTX-U) [Menard J *et al* 2012 *Nucl. Fusion* **52** 083015] show Electron Cyclotron Resonance Heating (ECRH) as an important component in preparing a target plasma for efficient High Harmonic Fast Wave and Neutral Beam heating. An extensive modelling effort of the propagation and absorption of EC waves in the evolving plasma is required to define the most effective window of operation, and to optimize the launcher geometry for maximal heating and current drive during this window. Here, we extend a previous optimization of O1-mode ECRH on NSTX-U to account for the full time-dependent performance of the ECRH using simulations performed with TRANSP, which self-consistently evolves the plasma equilibrium in time. It is found that time-dependent effects play a significant role in the effectiveness of the ECRH, particularly those related to the evolution of the density profile, which are not captured by analysis on static profiles. The optimal injection angle, pointed 3° above the poloidal midplane and 4° in the toroidal direction, belongs to a class of injection angles robust to alterations in the density rampup, making it useful for a broad range of experimental conditions.

Keywords: Electron Cyclotron, startup, spherical tokamaks

1. Introduction

Spherical tokamaks (STs)[, ,] are a promising fusion reactor design due to their reduced aspect ratio and increased plasma β, the ratio of plasma kinetic pressure to magnetic pressure. Compared to conventional tokamaks, STs feature improved MHD stability, and their projected higher neutron fluence makes them an attractive option for testing reactor components[,] or for use in fission-fusion hybrid designs[,].

The Princeton Plasma Physics Laboratory has recently completed an upgrade to their flagship ST, now NSTX-U (National Spherical Torus eXperiment Upgrade)[,]. By design, STs do not have much room for a central solenoid; a key mission goal of the NSTX-U experimental campaign is to therefore explore non-solenoidal startup and

operation. A promising technique for non-solenoidal startup is known as Coaxial Helicity Injection (CHI)[,], in which closed flux surfaces are formed by the DC injection of electrostatic helicity at the bottom of the vacuum vessel.

Past experiments conducted on NSTX utilizing CHI startup have produced up to 200 kA of initial toroidal current[, ,], and projections to NSTX-U predict that CHI start-up scenarios exceeding 400 kA should be attainable[ ]. An interesting ramp-up scheme has recently been proposed for use on STs in which CHI-produced plasmas are heated with radiofrequency (RF) waves to prepare a target plasma that can then be efficiently sustained by neutral beam injection and the self-generated bootstrap current[ ]. A key feature in this proposed technique is the improved coupling of the High Harmonic Fast Wave (HHFW) power to the bulk electron population through the pre-heating of electrons via Electron Cyclotron Resonance Heating (ECRH). Through this synergy, the HHFW current drive efficiency is predicted to increase substantially, by nearly a factor of 2 when the phasing of the HHFW launcher is chosen to inject waves with $k_{\parallel} = 3\ \mathrm{m}^{-1}$.

In part for this reason, a MW-level, 28 Ghz ECRH system is presently being designed for implementation on NSTX-U[, ,]. Initial experiments will focus on fundamental O-mode (O1-mode) EC heating and on the development of electron Bernstein wave (EBW) startup scenarios, as have been successfully demonstrated on MAST[,]. Future applications will explore the O-X-B double mode-conversion scheme[ ] as means to drive current when the plasma has grown overdense to traditional RF current drive techniques. Previous efforts to optimize the proposed ECRH system relied upon NSTX plasmas projected to NSTX-U; however, with NSTX-U operational, experimentally obtained plasma profiles can be used for more accurate optimization.

Moreover, the time-evolution of a plasma discharge is a highly coupled, multi-physics problem; a proper optimization scheme should therefore incorporate figures of merit that evaluate performance over the entire shot duration rather than at a single time. Specifically, an optimization of ECRH should consider the change in absorption properties of the target plasma as it evolves in response to the applied RF power. Similarly, during the startup phase the target plasma may move significantly as it settles to an equilibrium position within the vacuum chamber; for example, both traditional Ohmic discharges and CHI discharges tend to form closed flux surfaces near the bottom of the vacuum vessel, which then drift and expand upwards towards the midplane. A proper optimization scheme should consider the non-stationarity of the target plasma as well.

In this work, we present a feasibility study of O1-mode EC heating and current drive on NSTX-U at full field of 1 Tesla. This work extends a previous study of O1-mode ECRH on NSTX-U[ ] by incorporating the full time-dependent performance of the ECRH into the analysis. Integral to this study are time-dependent simulations performed with the transport solver TRANSP[ ], which self-consistently evolves the plasma equilibrium in the presence of the injected RF power. The EC heating and current drive calculations are performed with the ray tracing code GENRAY[,] as

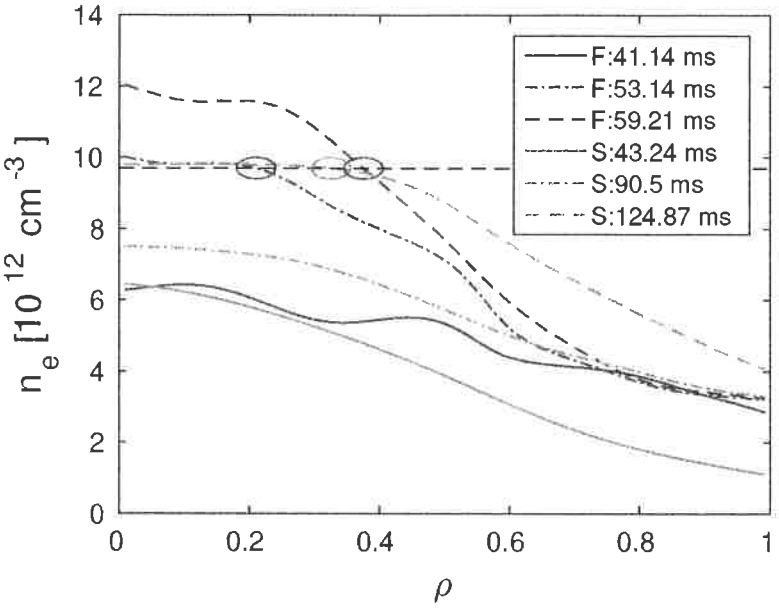

Figure 1. Density profiles at selected times for the fast rampup scenario (blue) and the slow rampup scenario (red). Shown in dashed black is the cutoff density for 28 GHz, 9.7×10^{12} cm^{-3}. For clarity, the locations where the density profiles cross the cutoff density are circled in their respective colors. The radial coordinate used is normalized toroidal flux coordinate $\rho \doteq \sqrt{\frac{\psi(r)}{\psi(a)}}$.

a coupled module within the TRANSP framework.

This paper is organized as follows: in section 2 we briefly describe the simulation setup used in this work. Section 3 presents the results of a broad scan over injection angle, introduces the Figure of Merit used to asses launcher performance, and discusses the results of the optimization. In particular, the optimization effort is decoupled from the choice of rampup scenario, such that the optimal injection angle is insensitive to the density evolution. Finally, section 4 provides final recommendations and discusses future work.

2. Simulation details

Previous ray tracing calculations[ ] concluded that the first-pass absorption (FPA) for O1-mode ECRH on NSTX-U is optimized at a launch angle of 5° downward and 1° in the toroidal direction with respect to the plasma normal. As this analysis was conducted for a static set of plasma parameters, it is unclear if the proposed launch angle will remain optimal throughout the EC phase as the plasma evolves in response to the injected EC power and as the changing density profile continuously modifies the accessibility of the ECRH. This launcher configuration has been used in time-dependent simulations[ ], which demonstrated that the ECRH is sufficient at heating the plasma during start-up. However, these simulations also indicated a need for current drive,

while the launcher configuration was optimized for pure heating. Therefore, increasing the EC current drive (ECCD) is a necessary goal of the new optimization effort.

The TRANSP simulations use the TEQ inverse solver[ ] for fixed-boundary equilibrium calculations, with NSTX-U shot #204202 as the reference. The MultiMode MMM7.1[ ] model is used to predict the electron and ion thermal transport, based on the assessment presented in ref. [ ]. The total plasma current is fully prescribed as a function of time by the experimental measurements. The non-inductive contribution is calculated with GENRAY using the Lin-Liu subroutine[ ] with momentum conserving corrections[ ] and then passed into the main TRANSP framework as input for the equilibrium calculations; the integral constraint imposed by the prescribed total current determines the ohmic contribution. Within GENRAY, the ECRH is modelled as a uniform beam that is initially laminar, launched from its focal point located on the midplane at $R = 2$ m with an initial divergence of 3.0°.

For this optimization study, two different rampup scenarios are considered for the density evolution. The first uses the density evolution of NSTX shot #140358. This scenario is henceforth referred to as the "slow density rampup" scenario, as the plasma becomes overdense after approximately 125 ms. For reference, the cutoff density at 28 GHz is 9.7×10^{12} cm^{-3}. The second scenario, conversely titled the "fast density rampup" scenario, uses the density profiles obtained from NSTX-U shot #204202. In this case, the density profile is highly peaked and exceeds the cutoff density at 53.14 ms. However, off-axis deposition remains effective until approximately 60 ms, when the density profile becomes overdense to a broader angular window. In both cases, the entire 2-D profiles are prescribed by the experimental measurements. The distinction between these two density rampup scenario is presented further in figure 1.

3. O1-mode ECRH Optimization

3.1. Angular scan details

To characterize the effect of injection angle on the EC power absorption and CD efficiency, an angular scan $\{(\phi, \theta) \mid \phi \in [0, 4]^\circ, \theta \in [-7, 7]^\circ\}$ has been conducted for each rampup scenario‡, where ϕ is taken with respect to the plasma normal and positive in the direction of the vacuum toroidal field, and θ is taken with respect to the geometric midplane, and is positive above the midplane. In these scans, only the first pass is considered; as such, for a divergence of 3.0°, the maximum toroidal injection angle is limited to 4°. This ensures the injected power does not pass tangential to the center stack and re-enter the plasma, contaminating the 'first pass' results output by GENRAY with an effective second pass.

The results of these scans are shown in figure 2. In the figure, the time-averaged ECCD and the FPA percentage for both rampup scenarios are shown as functions of

‡ We now use the notation (toroidal angle, poloidal angle) to describe the launch angle with respect to the plasma normal.

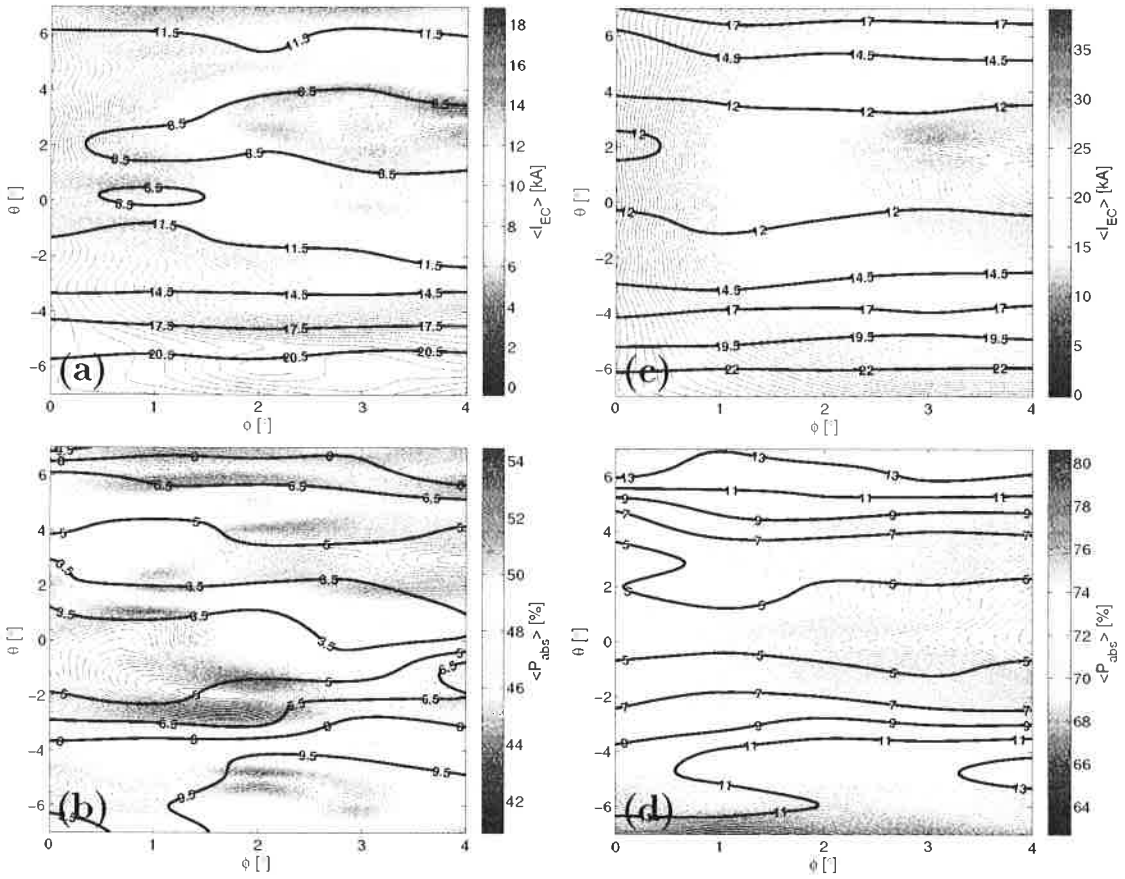

Figure 2. (a-b) Contour plots obtained for the fast density rampup scenario. (c-d) Contour plots obtained for the slow density rampup scenario. For both rampup scenarios, shown from top to bottom are the ECCD and the first-pass absorption percentage as functions of the injection angle. The black contours in the ECCD plots depict the time-averaged flux coordinate for the peak power deposition location, while the time-averaged FWHM for the power deposition is shown as the black contours in the absorption plots. The black contour labels are all re-scaled by a factor of 100 for convenience. All quantities are time-averaged, with time-intervals defined as [27, 60] ms and [27, 125] ms for the fast rampup and slow rampup scenarios, respectively.

the injection angle. The time-interval over which the time-averaging is performed is [27, 60] ms and [27, 125] ms for the fast and slow rampups respectively. Also shown as black contours in figure 2 are the results of fitting a gaussian profile to the EC power deposition profiles: the time-averaged flux coordinate for the peak deposition location is shown as the black contour lines in the ECCD plots, while the time-averaged Full Width at Half Maximum (FWHM) is shown as the black contour lines in the FPA plots. For convenience, both are re-scaled by a factor of 100.

As seen in figure 2, the FPA can be optimized for both rampup scenarios with launch angles within 4° above the poloidal midplane, and shifted at least 2° in the toroidal direction. This is in contrast to the previously recommended angle of $(1°, -5°)$ that was obtained based on single time-slice analysis. Furthermore, strong, on-axis

current drive can be expected within this angular region since, for EC waves with finite $n_\parallel$, high FPA is naturally accompanied by directed current drive[ ].

Notably, the plots in figure 2 are asymmetric with respect to the poloidal launch angle. There are two reasons for this: the finite pitch angle of the magnetic field and consequent asymmetry in the launched $k_\parallel$ spectrum of the EC waves, and the vertical displacement of the magnetic axis from the geometric axis.

Since the magnetic field lines are angled towards the $(-\phi, -\theta)$ quadrant, EC waves launched with $\theta > 0$ (θ^+ rays) have a smaller $k_\parallel$ than those launched with $\theta < 0$ (θ^- rays). When $k_\parallel$ is identically zero, O-mode is linearly polarized along the external magnetic field; however for finite $k_\parallel$, O-mode develops a small, left-hand circularly polarized component. Indeed, a quick calculation shows that for O-mode, the transverse polarization is given as:

$$\frac{iB_x}{B_y} = -\frac{\omega_{ce}}{\omega}\frac{(\omega^2 - \omega_{pe}^2)N_\parallel^2}{\omega_{ce}^2 N_\perp^2 + (\omega^2 - \omega_{pe}^2)N_\parallel^2} \tag{1}$$

For finite $N_\parallel$ in the regions of propagation, $\frac{iB_x}{B_y} < 0$, meaning the transverse polarization rotates in a left-handed sense. This polarization mis-match will reduce the electron cyclotron damping of these waves within the resonance region.

Furthermore, although the flux surfaces used in these simulations are up-down symmetric with respect to the magnetic axis, the magnetic axis is displaced vertically upward (~ 5 cm) from the geometric axis. Consequently, the angle between a launched ray bundle and $\nabla\psi$ will be larger for θ^- rays than for the θ^+ counterparts. Thus, θ^- rays will: (1) be aimed towards regions of lower electron temperature and density, (2) tend to deflect more towards the plasma periphery, (3) have a less desirable wave polarization at the resonance region compared to θ^+ rays; accordingly, θ^- rays have a lower power absorption efficiency. A smaller $k_\parallel$ will also reduce the Doppler effect experienced by the θ^+ rays compared to the θ^- rays. This will cause the deposition profiles for the θ^+ rays to be narrower and more localized on-axis, a trend corroborated by the black contours in figure 2.

An interesting feature of the fast rampup scenario is the appearance of a second angular region $\{(\phi, \theta) \mid \phi > 1^\circ, \theta > 4^\circ\}$ in which strong time-averaged FPA is also observed. This peak is not observed in the slow rampup case. The reason for this is entirely due to the manner in which the fast and slow density rampups approach the overdense regime. For the fast density rampup, the EC absorption suffers what can be considered reflection-dominated deterioration. This is to say, when the density profile grows overdense, the radial extent of the overdense region is localized to within $\rho \lesssim 0.2$. Being highly peaked, the density gradient is large near the axis and falls off with radius. For O-mode, both of these effects combine such that a small subset of the angular region located near the poloidal midplane is severely affected by the overdense region, while injection angles with larger poloidal component are somewhat less affected and can still damp effectively at larger radius. This is a small effect, but it acts to extend the window of operation for injections at larger poloidal angle, which in turn increases

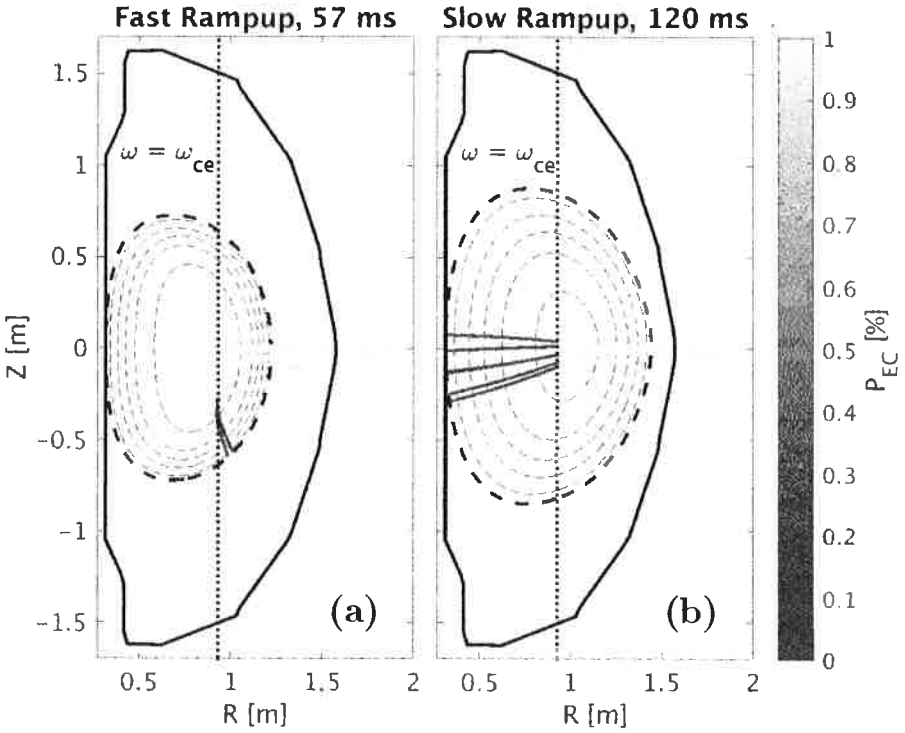

Figure 3. **(a)** Late-time behavior of the fast density rampup, characterized by reflection-dominated deterioration. High poloidal angles can deflect under the overdense core and reach the resonance layer, while low poloidal angles are reflected. **(b)** Late-time behavior of the slow density rampup, characterized by deflection-dominated deterioration. High poloidal angles are deflected away from the resonance layer, while low poloidal angles propagate relatively unimpeded.

the time-averaged FPA. Because the FPA for this angular region is not 'intrinsically' high, the ECCD is likewise not as high in this region.

On the other hand, the slow density rampup suffers from deflection-dominated deterioration. This limit is characterized by a density rampup that broadly surpasses the critical density, rather than narrowly. Therefore, all injection angles are cut off at nearly the same time. Moreover, as the density gradient is nearly constant spatially, the deflections experienced by each ray will be a monotonically increasing function of the poloidal injection angle. Consequently as the density ramps up, larger poloidal injection angles will suffer more detrimental effects associated with beam deflection than injection angles closer to the midplane. Both of these effects, summarized in figure 3, are crucial in understanding the late-time behavior of the FPA traces shown in figure 4.

It is important to remark that a similar effect does not occur with respect for the toroidal injection angle. In fact, the toroidal injection angle is largely insensitive to the differences in the density rampup. This is because of the small range of the toroidal angular scan, which is set by the beam divergence and the angular width of the center stack. Presumably, this effect would be present in the toroidal injection angle as well if

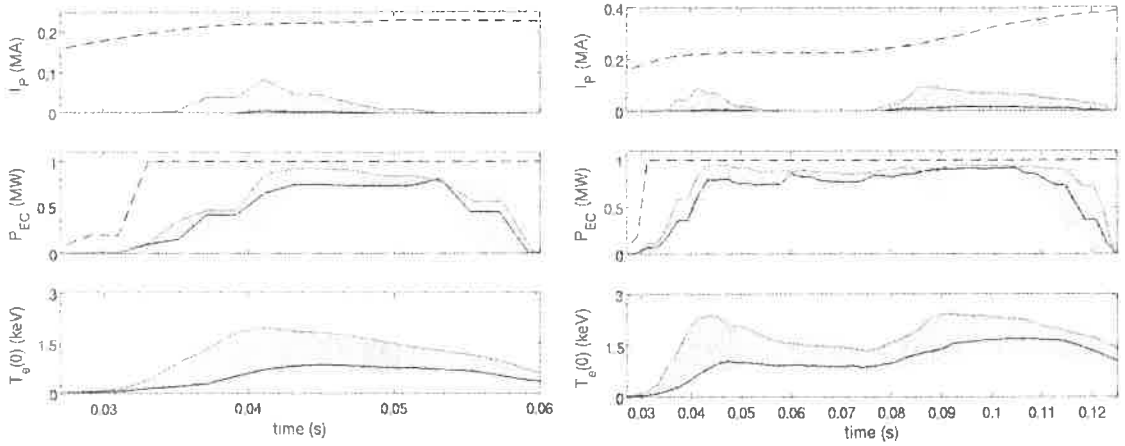

Figure 4. Comparison traces between $(1°, -5°)$ (black) and $(4°, 3°)$ (red) for the fast density rampup (left) and the slow density rampup (right). From top to bottom, the ECCD, and absorbed power and the central electron temperature are shown as functions of time. The black dashed lines in the I_p and P_{EC} traces correspond to the prescribed total current, and the injected EC power, respectively. The shaded blue envelope corresponds to the total possible range of performance when considering contributions from the entire angular scan.

larger injection angles were considered.

As a second remark, since the density evolution defines the window of operation for each injection angle separately, a proper ECRH optimization should compare angles with high intrinsic FPA against those with an extended window of operation. In the case that these constitute the same set of angles, such as in the slow density rampup, then this comparison is trivial. However, if these are not the same set of angles, as in the fast density rampup, then it may be the case that the optimal injection angle does not have the highest FPA while the plasma is underdense, but has the longest window of operation. This result cannot be obtained through analysis on a single time-slice.

3.2. Figure of Merit details and optimization results

An injection angle robust to modifications in the density evolution is preferable when the density evolution is an unknown quantity. For this purpose, the following Figure of Merit (FoM) is used to asses launcher performance:

$$\mathrm{FoM} = \frac{1}{6} \sum_{d=\mathrm{F,S}} \left(\langle \tilde{I}^d_{\mathrm{EC}} \rangle + \langle \tilde{P}^{\mathrm{d}}_{Abs} \rangle + \sqrt{\frac{\langle \tilde{\Delta}^d \rangle}{2}} - 6\delta^d \right) \tag{2}$$

where the summation is over the fast and slow density rampups, the angle brackets denote time-averaging, and for a given set of values $\mathbf{O} \doteq \{O_i\}$, we have defined $\tilde{O}_i \doteq O_i / \max(\mathbf{O})$. We also define $\langle \tilde{\Delta}^d \rangle \doteq \langle \tilde{\sigma}^d \rangle + 1$, where $\langle \tilde{\sigma}^d \rangle$ is time-averaged FWHM of the power deposition profile as obtained with a Gaussian fit. Lastly, we define $\delta^d \doteq \frac{1}{2}(N_{\mathrm{zone}} - 1)$, where N_{zone} is the minimum number of radial zones used in

Table 1. Top 5 injection angles as determined by applying equation 2 to the angular scan.

Angle	FoM
$(4°,\ 3°)$	0.925
$(4°,\ 0°)$	0.827
$(4°, -1°)$	0.817
$(3°, -1°)$	0.791
$(2°,\ 2°)$	0.781

the ECCD smoothing algorithm. Note that $N_{\text{zone}} = 1$ means no additional smoothing is added to the current profiles, so there is no penalty applied to the respective launch angle.

This FoM provides the simplest balance of performance on the two separate rampup scenarios. For stability considerations, the third term acts as a small penalty against narrow deposition profiles, while the final term is a harsh penalty against injection angles that require additional smoothing to reach convergence in the equilibrium calculations. Applying equation 2 to the angular scan, the recommended ECRH injection angle that maximizes the FoM is $(4°, 3°)$. For reference, the top 5 scoring injection angles are shown in table 1.

Figure 4 compares the full time-dependent performance of the angle $(4°, 3°)$ with the previously recommended angle $(1°, -5°)$ for both rampup scenarios. The quantities shown in the figure are the ECCD, the FPA, and the central electron temperature as functions of time. Furthermore, the light blue region enveloping the traces depicts the total possible range of performance resulting from the angular scan. To prevent misinterpretations of this envelope, we emphasize that the physical trajectories through this 'performance' space are non-trivial and non-monotonic. In order to follow a constant trajectory, such as attaining the maximum possible performance over the entire EC phase, one would need to dynamically change the EC injection angle in response to the plasma evolution.

For the fast density rampup, the windows of operation for the angles $(1°, -5°)$ and $(4°, 3°)$ are comparable; however, $(4°, 3°)$ has a slightly extended window on the slow rampup due to the effects of deflection-dominated deterioration. Therefore, we see that because of its intermediate poloidal injection angle, $(4°, 3°)$ optimally balances the detriments of reflection- and deflection-dominated deterioration. Additionally, the angle $(4°, 3°)$ provides highly localized on-axis heating, allowing central electron temperatures up to 1.96 keV and 2.42 keV for the respective fast and slow rampup scenarios. The large toroidal injection angle combined with high FPA allows for non-inductive current exceeding 84 kA and 92 kA to be obtained on the fast and slow rampups. A more detailed comparison of the two injection angles is shown in table 2, and deposition profiles at selected times can be viewed in figure 5.

In producing figure 5, an averaging is performed over a small range of selected time-slices. For the slow rampup, the averaging is performed over the time periods

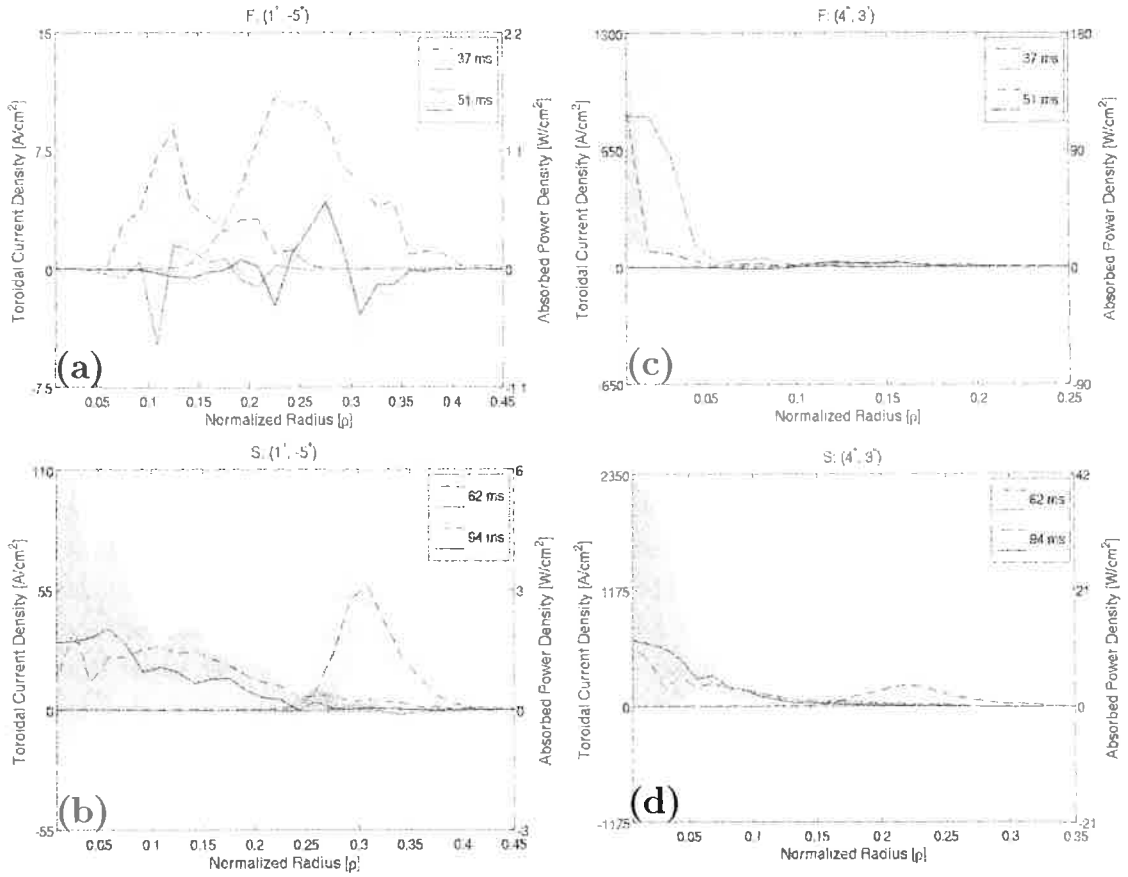

Figure 5. Radial profiles for the mean EC current density (red/blue solid lines) and the mean EC absorbed power density (pink/cyan dashed lines) at selected times. For the slow density case, the averaging is performed over the time periods [56, 68] ms and [88, 100] ms, while for the fast density case, the time periods are [35, 39] ms and [49, 53] ms. Shown in the figure legend are the central times for these intervals. The shaded envelope depicts the total variation in the respective profile over the time periods. Subplots (a,b) correspond to the previously recommended angle $(1°, -5°)$, while subplots (c,d) correspond to the angle $(4°, 3°)$, both for the fast and slow density rampups respectively.

[56, 68] ms and [88, 100] ms, while for the fast rampup, the time periods are [35, 39] ms and [49, 53] ms. In both cases, the width of the averaging region constitutes 12% of the ECRH duration. The central times for the slow rampup were selected to sample the peak and valley regions of the EC current profile, whereas the central times for the fast rampup were chosen to show the early- and late-time behavior of the ECRH, when the reflection-dominated deterioration is not and is present.

The deposition of $(1°, -5°)$ tends to be spread out over a large radial region, with the current profile rapidly oscillating about zero such as to yield negligible net current. On the contrary, the deposition of $(4°, 3°)$ is well-localized within $\rho = 0.25$. A notable exception occurs in the vicinity of 60 ms on the slow rampup, in which the deposition location for all injection angles shifts outward. The highly peaked heating and current

Table 2. Comparison between the originally proposed injection angle of $(1°, -5°)$ and the injection angle $(4°, 3°)$. Notationally, we have introduced ρ_0 as the radial location of the maximum power deposition.

	$(1°, -5°)$		$(4°, 3°)$	
	Fast	Slow	Fast	Slow
$\max(FPA)$ [%]	80.99	92.31	92.47	95.20
$\langle FPA \rangle$ [%]	45.24	68.66	54.37	79.37
$\max(I_{\mathrm{EC}})$ [kA]	5.30	17.35	84.21	92.27
$\langle I_{\mathrm{EC}} \rangle$ [kA]	0.78	5.36	18.99	35.03
$\max(T_e(0))$ [keV]	0.86	1.71	1.96	2.42
$\langle T_e(0) \rangle$ [keV]	0.51	1.08	1.16	1.75
$\max(\rho_0)$ $[10^{-2}]$	36.45	34.03	26.18	26.07
$\min(\rho_0)$ $[10^{-2}]$	10.17	1.47	0.00	0.00
$\langle \rho_0 \rangle$ $[10^{-2}]$	19.40	19.10	7.60	11.42
$\max(\sigma)$ $[10^{-2}]$	13.60	24.72	10.50	12.36
$\min(\sigma)$ $[10^{-2}]$	2.55	1.98	0.19	2.22
$\langle \sigma \rangle$ $[10^{-2}]$	8.69	11.13	4.49	5.73
δ	0	0	0	0
FoM	0.626		0.925	

profiles associated with $(4°, 3°)$ beg the question of MHD stability. For this purpose, equilibria from selected times were analyzed with the linear MHD codes BALLOON[ ] and PEST[ ] and found to be linearly stable to ballooning and kink modes.

Finally, the two peaks present in the I_p and $T_e(0)$ traces for the slow density rampup merit brief discussion. Both the ECCD and the central electron temperature rise initially; however, beginning around 50 ms until approximately 80 ms, both suffer significant reductions in magnitude before recovering. As seen in figure 6, this time period coincides with an inward transit of the plasma flux surfaces. The magnetic axis, initially located at $R = 0.92$ m, shifts to a minimum distance of $R = 0.82$ m before moving outwards and approaching $R = 1.02$ m.

A possible mechanism to link the two-peaked I_p and $T_e(0)$ traces to the shifting plasma is given by the following argument: consider the single particle non-relativistic EC resonance condition, which can be written as:

$$v_{\parallel} = \frac{\omega - \omega_{ce}}{k_{\parallel}} \tag{3}$$

As such, resonant particles are required to have larger values of $v_{\parallel}$ the farther they are from the resonance layer $\omega = \omega_{ce}$. Since effective ECCD relies on the EC waves damping on particles with finite $v_{\parallel}$, it likewise relies upon a strong Doppler shift present in the deposition profile.

In figure 6, the magnetic axis begins at the resonance layer and shifts to the High-Field Side (HFS). At this time, the electron temperature is a centrally-peaked function of ρ, so the resonance layer shifts into a colder region of the plasma with a larger spatial

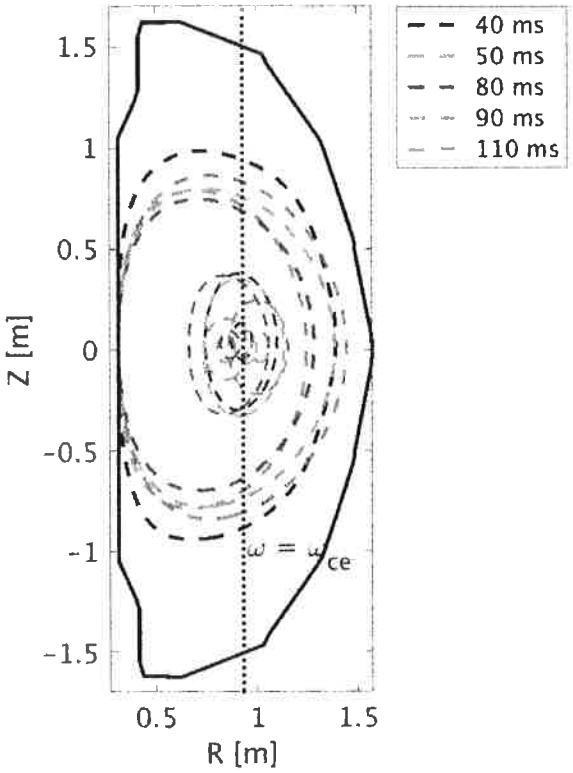

Figure 6. Snapshots of the inner plasma flux surfaces at selected times. The flux surfaces shown are $\rho = 1.0$ (bold), $\rho = 0.1$, and $\rho = 0.01$. An inward shift of the inner flux surfaces appears during a time period contemporaneous with the observed deterioration of the ECCD in the slow density rampup scenario; the resurgence of the ECCD coincides with the flux surfaces returning to their original location.

temperature gradient. This in turn acts to reduce the Doppler effect on the incoming side of the resonance and to increase the Doppler effect on the outgoing side, resulting in partial cancellation of the driven current. This partial cancellation is further augmented by the continued inward transit of the plasma until negligible net current results. The diminution of the central electron temperature simply reflects the change in deposition location as the plasma shifts laterally, as seen in Fig 5.

We emphasize that *all* injection angles suffer a reduced ECCD efficiency at this time. For this reason, one cannot remedy the drop in efficiency by dynamically updating the EC injection angle to a new injection angle of the scanned set. If high ECCD efficiency is to be maintained throughout the EC duration, feedback stabilizing mechanisms should be utilized to prevent the magnetic axis from shifting inward.

4. Conclusion

In this work, we assess the feasibility of ECRH on NSTX-U using time-dependent simulations. For traditional O1-mode ECRH, two separate density rampup scenarios are considered: a fast rampup in which the plasma becomes overdense at approximately 60 ms, and a slower rampup where the plasma becomes overdense at approximately 125 ms. An angular scan is performed over the poloidal and toroidal injection angles, and it is found that there exists a broad angular region robust to modifications in the density rampup. In this region, the injection angle is shifted at least 2° in the toroidal direction and within 4° above the poloidal midplane.

For the optimization, a simple Figure of Merit is developed that balances the current drive and the first pass absorption achieved by each injection angle over the entire EC duration. Applying this Figure of Merit to the angular scan, the optimal injection angle points 3° above the poloidal midplane and 4° in the toroidal direction, which belongs to the identified class of robust injection angles.

For this optimal choice of injection angle, the deposition is peaked on-axis and as such, central electron temperatures exceeding 1.9 keV and 2.4 keV can be obtained for the fast and slow rampup scenarios, respectively. Additionally, this injection angle can provide up to 84 kA of ECCD on the fast rampup and 92 kA on the slow rampup cases. This achieved heating and current drive will be integral in the development of non-inductive startup, rampup, and sustainment scenarios on next-generation spherical tokamaks. However, deleterious effects associated with an inward transit of the plasma flux surfaces are observed in the slow density rampup, which result in the EC current drive efficiency dropping substantially. Such motion of the plasma should thus be minimized in future experiments to maximize the ECCD efficiency.

A notable finding in this study is the effect of the density evolution on the time-averaged EC power absorption. In the fast rampup scenario, the density evolution acts to reduce the accessibility of EC rays launched with low poloidal injection angles; conversely in the slow rampup scenario, the density evolution limits the accessibility of EC rays launched with large poloidal injection angles. The former we categorize as a "reflection-dominated" density evolution, and the later as a "deflection-dominated" density evolution. In light of this, the injection angle $(4°, 3°)$ is robust to variations in the density evolution as it belongs to a class of intermediate poloidal injection angles that provides an optimal balance between the two effects. The quantification of these late-time density effects should facilitate the development of a controller equation for adjusting the EC injection angle given details of the density rampup. This will be the subject of a future publication.

Acknowledgments

The authors would like to thank G. Taylor, Y. Petrov, and R. Harvey for helpful discussion. This work is supported by DOE contract DEAC02-09CH11466.

References

[1] Peng Y K and Strickler D 1986 *Nuclear Fusion* **26** 769

[2] Stambaugh R D, Chan V S, Miller R L and Schaffer M J 1998 *Fusion Science and Technology* **33** 1

[3] Jardin S, Kessel C, Menard J, Mau T, Miller R, Najmabadi F, Chan V, Lao L, Lin-liu Y, Miller R, Petrie T, Politzer P and Turnbull A 2003 *Fusion Engineering and Design* **65** 165

[4] Peng Y K M, Fogarty P J, Burgess T W, Strickler D J, Nelson B E, Tsai J, Neumeyer C A, Bell R, Kessel C, Menard J, Gates D, LeBlanc B, Mikkelsen D, Fredrickson E, Grisham L, Schmidt J, Rutherford P, Sabbagh S, Field A, Sykes A, Cook I, Mitarai O and Takase Y 2005 *Plasma Physics and Controlled Fusion* **47** B263

[5] Peng Y K M, Burgess T W, Carroll A J, Neumeyer C L, Canik J M, Cole M J, Dorland W D, Fogarty P J, Grisham L, Hillis D L, Katoh Y, Korsah K, Kotschenreuther M, LaHaye R, Mahajan S, Majeski R, Nelson B E, Patton B D, Rasmussen D A, Sabbagh S A, Sontag A C, Stoller R E, Tsai C C, Valanju P, Wagner J C and Yoder G L 2009 *Fusion Science and Technology* **56** 957

[6] Kotschenreuther M, Valanju P, Mahajan S and Schneider E 2009 *Fusion Engineering and Design* **84** 83

[7] Gryaznevich M P 2012 *AIP Conference Proceedings* **1442** 55

[8] Menard J, Gerhardt S, Bell M, Bialek J, Brooks A, Canik J, Chrzanowski J, Denault M, Dudek L, Gates D, Gorelenkov N, Guttenfelder W, Hatcher R, Hosea J, Kaita R, Kaye S, Kessel C, Kolemen E, Kugel H, Maingi R, Mardenfeld M, Mueller D, Nelson B, Neumeyer C, Ono M, Perry E, Ramakrishnan R, Raman R, Ren Y, Sabbagh S, Smith M, Soukhanovskii V, Stevenson T, Strykowsky R, Stutman D, Taylor G, Titus P, Tresemer K, Tritz K, Viola M, Williams M, Woolley R, Yuh H, Zhang H, Zhai Y, Zolfaghari A and the NSTX Team 2012 *Nuclear Fusion* **52** 083015

[9] Menard J 2015 *Bull. Am. Phys. Soc.* **60** 14 Abstract B3.00001

[10] Jenson T H and Chu M S 1984 *Phys. Fluids* **27** 2881

[11] Jarboe T R 1989 *Fusion Science and Technology* **15** 7–11

[12] Raman R, Mueller D, Nelson B A, Jarboe T R, Gerhardt S, Kugel H W, LeBlanc B, Maingi R, Menard J, Ono M, Paul S, Roquemore L, Sabbagh S and Soukhanovskii V 2010 *Phys. Rev. Lett.* **104** 095003

[13] Nelson B, Jarboe T, Mueller D, Raman R, Bell M, Menard J, Ono M, Roquemore A, Soukhanovskii V, Yuh H and the NSTX Research Team 2011 *Nuclear Fusion* **51** 063008

[14] Raman R, Mueller D, Jarboe T R, Nelson B A, Bell M G, Gerhardt S, LeBlanc B, Menard J, Ono M, Roquemore L and Soukhanovskii V 2011 *Physics of Plasmas* **18** 09254

[15] Raman R, Mueller D, Jardin S, Jarboe T, Nelson B, Bell M, Gerhardt S, Hooper E, Kaye S, Kessel C, Menard J, Ono M, Soukhanovskii V and the NSTX Research Team 2013 *Nuclear Fusion* **53** 073017

[16] Poli F, Andre R, Bertelli N, Gerhardt S, Mueller D and Taylor G 2015 *Nuclear Fusion* **55** 123011

[17] Taylor, G, Ellis, RA, Harvey, RW, Hosea, JC and Smirnov, AP 2012 *EPJ Web of Conferences* **32** 02014

[18] Taylor, G, Ellis, RA, Fredd, E, Gerhardt, S P, Greenough, N, Harvey, R W, Hosea, J C, Parker, R, Poli, F, Raman, R, Shiraiwa, S, Smirnov, A P, Terry, D, Wallace, G and Wukitch, S 2015 *EPJ Web of Conferences* **87** 02013

[19] Kariya T, Minami R, Imai T, Kato T, Idei H, Hanada K, Zushi H, Numakura T, Endo Y and Ichimura M 2015 *Fusion Science and Technology* **68** 147

[20] Shevchenko V, O'Brien M, Taylor D, Saveliev A and MAST team 2010 *Nuclear Fusion* **50** 022004

[21] Shevchenko, VF, Baranov, YF, Bigelow, T, Caughman, JB, Diem, S, Dukes, C, Finburg, P, Hawes, J, Gurl, C, Griffiths, J, Mailloux, J, Peng, M, Saveliev, AN, Takase, Y, Tanaka, H and Taylor, G 2015 *EPJ Web of Conferences* **87** 02007

[22] Preinhaelter J and Kopecky V 1973 *J. Plasma Phys.* **10** 1

[23] Hawryluk R J 1981 An empirical approach to tokamak transport *Physics of Plasmas Close to Thermonuclear Conditions* vol 1 ed Coppi B, Leotta G G, Pfirsch D, Pozzoli R and Sindoni E (Brussels: Commission of the European Communities) p 19
[24] Smirnov A P and Harvey R W 1995 *Bull. Am. Phys. Soc.* **40** 1837 Abstract 8P35
[25] Smirnov A P, Harvey R W and Prater R 2009 General linear RF-current drive calculation in toroidal plasma *Proc. 15th Workshop on ECE and ECRH* (Singapore: World Scientific) p 301
[26] Andre R, McCune D, Pearlstein D, LoDestro L and Meyer W H 2007 *Bull. Am. Phys. Soc.* **52** 11 Abstract UP8.00082
[27] Rafiq T, Kritz A H, Weiland J, Pankin A Y and Luo L 2013 *Phys. Plasmas* **20** 032506
[28] Lin-Liu Y R, Chan V S and Prater R 2003 *Phys. Plasmas* **10** 4064
[29] Marushchenko N B, Beidler C D, Kasilov S V, Kernbichler W, Maassberg H, Prater R and Harvey R W 2011 *Phys. Plasmas* **18** 032501
[30] Eldridge O C 1980 *Oak Ridge National Laboratory Report* **ORNL/TM-7503** 6821959
[31] Chance M S, Kessel C and Jardin S C 1999 *Plasma Phys. Control. Fusion* **41** 1379
[32] Grimm R C, Greene J M and Johnson J L 1976 *Methods Comput. Phys.* **16** 253

PPPL PRINCETON PLASMA PHYSICS LABORATORY

Princeton Plasma Physics Laboratory
Office of Reports and Publications

Managed by
Princeton University

under contract with the
U.S. Department of Energy
(DE-AC02-09CH11466)

P.O. Box 451, Princeton, NJ 08543
Phone: 609-243-2245
Fax: 609-243-2751

E-mail: publications@pppl.gov

Website: http://www.pppl.gov